Tunable topological interface states and resonance states of surface waves based on the shape memory alloy

Shao-Yong Huo(霍绍勇)[1], Long-Chao Yao(姚龙超)[1], Kuan-Hong Hsieh(谢冠宏)[2], Chun-Ming Fu(符纯明)[1,†], Shih-Chia Chiu(邱士嘉)[2,‡], Xiao-Chao Gong(龚小超)[2], and Jian Deng(邓健)[1]

[1] *College of Mechanical Engineering, University of South China, Hengyang* 421001, *China*
[2] 1*MORE INC, Shenzhen* 518000, *China*

(Received 10 May 2022; revised manuscript received 10 July 2022; accepted manuscript online 5 August 2022)

Topological interface state (TIS) of elastic wave has attracted significant research interest due to its potential prospects in strengthening acoustic energy and enhancing the signal accuracy of damage identification and quantification. However, previous implementations on the interface modes of surface waves are limited to the non-adjustable frequency band and unalterable mode width. Here, we demonstrate the tunable TIS and topological resonance state (TRS) of Rayleigh wave by using a shape memory alloy (SMA) stubbed semi-infinite one-dimensional (1D) solid phononic crystals (PnCs), which simultaneously possesses the adjustable mode width. The mechanism of tunability stems from the phase transformation of the SMA between the martensite at low temperature and the austenite at high temperature. The tunable TIS of Rayleigh wave is realized by combining two bandgap-opened PnCs with different Zak phases. The TRS with adjustable mode width is achieved in the heterostructures by adding PnCs with Dirac point to the middle of two bandgap-opened PnCs with different Zak phases, which exhibits the extraordinary robustness in contrast to the ordinary Fabry–Pérot resonance state. This research provides new possibilities for the highly adjustable Rayleigh wave manipulation and find promising applications such as tunable energy harvesters, wide-mode filters, and high-sensitivity Rayleigh wave detectors.

Keywords: tunable topological interface state, Rayleigh wave, alterable mode width, topological phononic crystals, shape memory alloys

PACS: 43.55.+p, 43.90.+v, 02.40.Pc, 46.40.–f **DOI:** 10.1088/1674-1056/ac8727

1. Introduction

In recent years, the concepts in topological technologies such as the quantum Hall effect (QHE),[1] quantum spin Hall effect (QSHE),[2] quantum valley Hall effect (QVHE),[3] and Weyl semimetals,[4,5] have opened a new chapter of bosonic and classical waves with topology as the central principle. Owing to the topologically nontrivial nature of the underlying bands, the topologically protected edge/interface modes at domain walls between two crystals with opposite topological invariants have been found and exhibit the unique properties of being immune to backscattering from defects or disorders making them robust against structural perturbations.[6–15] Such edge/interface modes have shown excellent potentials for many engineering fields including the spintronics and quantum computation,[16] electromagnetic/acoustic wave communication,[17–19] nondestructive testing, and the design of modern biomedical devices.[20–22]

For one-dimensional (1D) periodic systems, the topological invariant of Bloch bands is the well-known Zak phase, which was initially proposed to characterize the bands of electron motions in 1D periodic solids.[23] The different configurations can be described by different values of the Zak phase, which is similar to the Su–Schrieffer–Heeger (SSH) model of polyacetylene.[24] Since then, this topological description of Zak phase has been extended into various classical wave systems such as 1D photonic crystals and phononic crystals (PnCs), which was successfully used to predict the existence of topological interface state (TIS). Xiao *et al.*[25] introduced the the concept of Zak phase into the 1D periodic acoustic system, and investigated the band inversion and experimentally confirmed the appearance of the acoustic TIS. Meng *et al.*[26] proposed a way of full phase diagrams in the parameter space to realize the acoustic TIS in arbitrary bandgap. Fan *et al.*[27] studied the possibility between the Zak phase and local resonance of two types of scatterers in the acoustic metamaterials. Huang *et al.*[28] have theoretically explored the TIS of shear horizontal wave with the Zak phase in the periodic plate system, in which they demonstrated that the TIS could be resulted from both Bragg scattering and local resonances. Jin *et al.*[29,30] demonstrated a kind of asymmetric robust TIS in the 1D PnC beam combining the Fano resonance and symmetry principle. Meanwhile, due to the main disadvantages of narrow working range with the single frequency points for the TIS in the previous 1D topological PnC systems, a theme of studying tunable TIS to realize the controllable and programmable wave manipulation has drawn increasing attention. Zhou *et*

[†]Corresponding author. E-mail: fuchunming@hnu.edu.cn
[‡]Corresponding author. E-mail: gary.sc.qiu@tiinlab.com

© 2023 Chinese Physical Society and IOP Publishing Ltd

al.[31–33] proposed a 1D active topological PnCs made of a homogeneous central epoxy central beam/rod sandwiched by two piezoelectric beams/rods, in which the tunable TIS could be realized by adjusting the capacitors of the periodic electric circuits. Chen *et al*.[34] demonstrated low-frequency tunable TIS for longitudinal wave by utilizing soft topological phononic crystals, in which the tunability is achieved based on the applied axial force field. Wang *et al*.[35] investigated the topological interface mode in a 1D granular PC composed of two sub-lattices, which can be tuned by varying the pre-compression between the spheres. By introducing the intelligent magnetoelastic materials, Feng *et al*.[36] demonstrated magnetically tunable topological interface states for Lamb waves in 1D PnC slabs. Although all the previous mentioned works demonstrate the tunability of TIS in the finite thickness PnC plate/beam system, a tunable TIS for surface acoustic wave in half-space has not yet been implemented. Different from the previous studies in tunable topological state by using the mechanical loading, external electric and magnetic fields, this work would propose another way to realize the tunability of TIS based on the shape memory alloy (SMA).[37–42]

SMA, as a special energy transduction material, exhibits the unique thermal and mechanical behaviors, which was widely investigated in vibration control of flexible structures as active actuators.[43–45] The mechanism behind the unique properties is based on the phase transformation between the martensite at low temperature and the austenite at high temperature for the SMA. The peculiar elastic modulus change caused by the crystallographic structure evolution would contribute to a controllable microstructure design.[46] In this paper, by utilizing the SMA based tunable surface wave PnCs, the adjustable TIS of Rayleigh wave is realized in the 1D periodic semi-infinite solid system. The underlying mechanism stems from the unique elastic modulus change of the SMA material induced by the phase transformation under a temperature load. Significantly, based on the tunable TIS of surface wave, a novel sandwich-like topological structure is further designed to realize the topological resonance state (TRS) in the 1D surface wave system by arranging the 1D PnC with Dirac point into the middle of two 1D PnCs possessed different Zak phase of bandgap. The obtained TRS of surface wave possesses the behavior of tailorable mode width that can well confine the surface wave displacement fields with desirable width. This work highlights the two advantages of tunability and mode width degree of freedom for surface wave TIS, which would find wide engineering applications in intelligent technologies needing controllable information processing, strengthening surface acoustic energy and topological channel with tailorable mode confinement.

2. Design of the tunable TIS of surface wave based on SMA

2.1. Model and design

The model of tunable topological surface wave considered here is constructed by arranging a periodic array of SMA surface layer on a soft epoxy substrate as shown in Fig. 1(a). A unit cell with lattice constant $a = 40$ mm is outlined by the red dashed rectangular strip. The surface structure of SMA is made up of the thin plate attached with semicircular block. The thicknesses of thin plate is $h_0 = 4$ mm and the radius of semicircular block is $R = 13.5$ mm. The epoxy substrate is much larger than that of the SMA surface layer so that it can be approximately seen as a half-space. The SMA, as one class of smart materials, possesses the significant phase transformation phenomenon between martensitic state and austenitic state under a temperature variation, which provided a convenience for designing the tunable topological interface states. The material characteristic between low temperature induced twin martensite phase and high temperature induced austenite phase is considered according to existing literature.[43–47] When an internal state variable of the martensitic fraction is defined as κ, the transformation from the current phase κ_0 to twinned martensite at the low temperature T ($M_\mathrm{f} \le T \le M_\mathrm{s}$) can be written by[48]

$$\kappa = \frac{1-\kappa_0}{2}\left[\cos\left(\pi\frac{T-M_\mathrm{f}}{M_\mathrm{f}-M_s}\right)+1\right], \tag{1}$$

where M_s and M_f are the starting and finishing temperatures of transition, respectively. Meanwhile for the high temperature ($A_\mathrm{s} \le T \le A_\mathrm{f}$), the the reverse transformation from the martensitic phase to the austenitic phase can be described by

$$\kappa = \frac{\kappa_0}{2}\left[\cos\left(\pi\frac{T-A_\mathrm{s}}{A_\mathrm{f}-A_\mathrm{s}}\right)+1\right], \tag{2}$$

where A_s and A_f are the transition temperatures of martensite starting and finishing, respectively. The elastic modulus of SMA is related to the fraction κ of martensite, which can be expressed by the following expression:

$$E_\mathrm{SMA} = E_\mathrm{A} + \kappa(E_\mathrm{M} - E_\mathrm{A}), \tag{3}$$

where E_A and E_M are the elastic modulus of fully martensitic and fully austenitic phases, respectively. It can be obtained that the elastic modulus of SMA presents a quasilinear relationship with temperature in the phase transition zone.[45,49]

Here, the material of SMA is chosen as NiTi and the corresponding material parameters of fully martensitic and fully austenitic phases are given in Table 1. The unit cells for martensite and austenite are displayed in Fig. 1(b), both of which are defined as type-I with the geometric center lying on the semicircle block. For the SMA of NiTi, it could be known that the temperature parameters M_s, M_f, A_s, and A_f are 295 K, 291 K, 308 K, and 318 K, respectively.[47] Since

the transition zone is a little narrow and hard to catch for the SMA of NiTi, we focus the research effort on demonstrating the tunable properties of topological surface wave localization and only the topological surface PnC structures in the fully martensitic and austenitic state are considered.

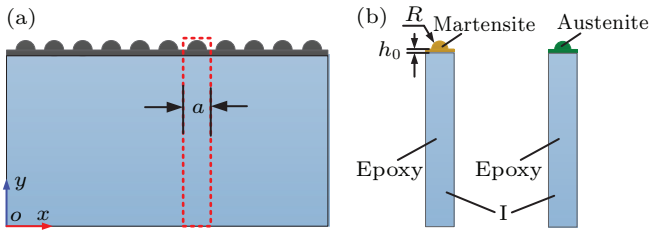


Fig. 1. (a) Schematics of 1D tunable elastic PnC for surface wave, in which the shape memory alloys is periodically arranged in the matrix of epoxy. (b) The structural models of the unit cell in the martensite phase state and austenitic phase state, respectively.

Table 1. Material parameters.

Materials	Young's modulus E (GPa)	Poisson's ratio (σ)	Mass density ρ (kg/m^3)
Epoxy	3.1	0.33	1180
Martensite	20	0.35	6000
Austenite	80	0.35	6000

2.2. Tunable topological bandgap of Rayleigh wave

To start with, we consider the band structures of the unit cell of type-I for the 1D surface wave PnCs. The finite element method (FEM) is employed to simulate the band structure. When performing it, the Floquet periodic boundary conditions are applied to left and right boundaries and the fixed boundary condition is applied to the bottom boundary. When the radius of semicircular block is $R = 13.5$ mm, the band structures of the Rayleigh wave PnCs in different material phase states are shown in Fig. 2. The shaded black dots present the bulk wave, and the marked red and blue dots presents the Rayleigh wave bands. The Rayleigh wave could be distinguished by energy distribution of each eigenmode. Figure 2(a) denotes the band structure of the unit cell in the martensite phase state, whereas figure 2(b) denotes the dispersion relation of the unit cell in the austenite phase state. It can be seen that the bandgaps of Rayleigh wave are formed in both cases. The band structure of Rayleigh wave in full martensite state with a lower elastic modulus formed a bandgap appearing from 6.5 kHz to 7.25 kHz. However, when the SMA of NiTi is transformed to the full austenite with a larger elastic modulus, the bandgap shifted upwards to a higher frequency range from 7.33 kHz to 8.715 kHz. Such an obvious shift on the frequency range indicates the tunable property of the bandgap in the proposed SMA surface wave PnCs, which also reveals that it is feasible to adaptively control the Rayleigh waves using the SMA designs by adjusting the thermal loads on the phase changing element.

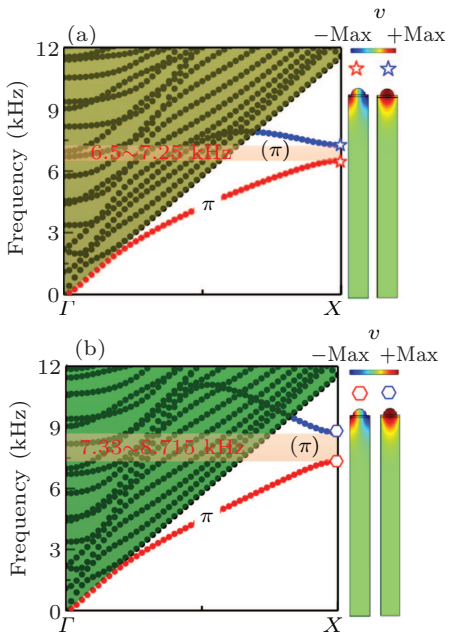


Fig. 2. (a) Band structure and geometrical topological phase of Rayleigh waves of the unit cell in the martensite phase state where the frequency range of the first topological band gap is 6.5 kHz–7.25 kHz. (b) Band structure and geometrical topological phase of Rayleigh waves of the unit cell in the austenite phase state where the frequency range of the first topological band gap is 7.33 kHz–8.715 kHz.

To investigate the topological property of the bandgap, we extend the concept of the Zak phase to surface wave systems. As a special type of topological invariant defined for 1D periodic systems, the Zak phase characterizes the topology of the Bloch bands. For the Rayleigh wave, the Zak phase for the n-th isolated pass band can be defined as[50]

$$\theta_n^{\mathrm{Zak}} = \int_{-\pi}^{\pi} \mathrm{i}\frac{1}{\Delta(k)} \times \left[\iint_S \left(U^*_{1(n,k)} \frac{\partial}{\partial k} U_{1(n,k)} + U^*_{2(n,k)} \frac{\partial}{\partial k} U_{2(n,k)} \right) \mathrm{d}S \right] \mathrm{d}k, \tag{4}$$

in which $\Delta(k) = \iint_s (U^*_{1(n,k)} U_{1(n,k)} + U^*_{2(n,k)} U_{2(n,k)}) \mathrm{d}S$. Meanwhile, $U_{1(n,k)}$ and $U_{1(n,k)}$ represent the periodic-in-cell part of displacement along x and y directions, respectively. As the unit cell possesses inversion symmetry with respect to its central cross-sectional plane, the geometric Zak phase can only take two values: either 0 or π. Another simple way to obtain the Zak phase of an isolated pass band by measuring the symmetry of the band edge states with the FEM. If the symmetry of both the band edge mode at $k = 0$ and $k = \pi/a$ are same, the Zak phase of the band is 0; and if the symmetry of the two band edge modes are different, the Zak phase of the band is π.[28] In the right panels of Figs. 2(a) and 2(b), the displacement field of the Rayleigh wave at $k = \pi/a$ are displayed. They are odd symmetric for the first pass band and that are even symmetric for second pass band. Since the symmetry of first surface wave pass band at $k = 0$ is even, both of the martensite's and austenite's Zak phases of the first pass band for type-I unit cell are π. Therefore, the Zak phases of the bandgaps for the martensite and austenite states are both π as shown in Fig. 2.

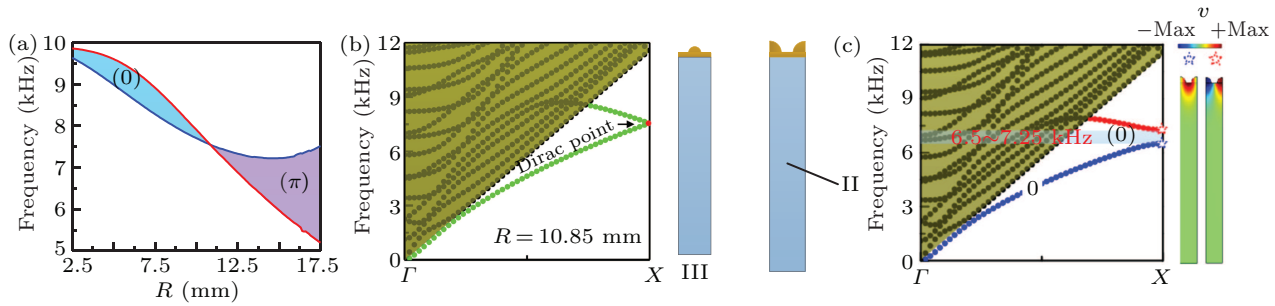


Fig. 3. (a) The eigenfrequency of eigenstates bounding the first band gap at the boundary of the Brillouin zone with the change of the geometric parameter R for the martensite phase state. (b) The band structure in case of Dirac point for the martensite phase state when geometric parameter $R = 10.85$ mm. (c) When the inversion center of unit cell is moved by $a/2$, the unit cell is defined as type-II and its band structure and geometrical topological phase of Rayleigh waves in the martensite phase state are displayed.

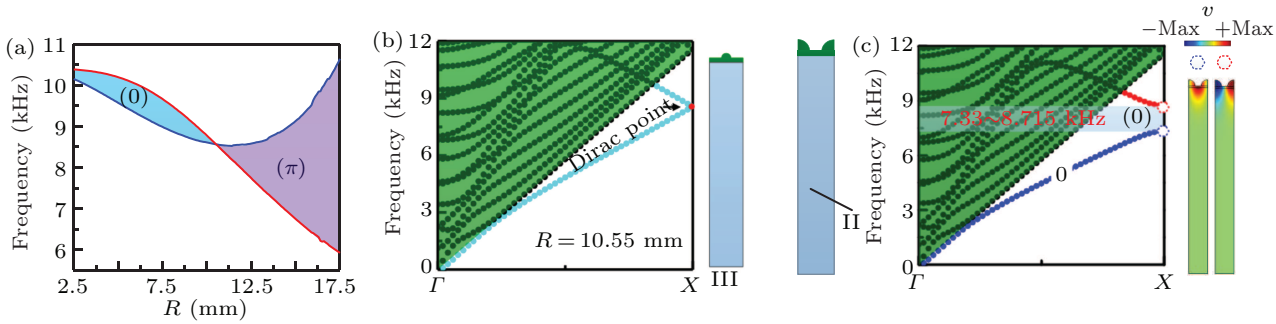


Fig. 4. (a) The eigenfrequency of eigenstates bounding the first band gap at the boundary of the Brillouin zone with the change of the geometric parameter R for the austenite phase state. (b) The band structure in case of Dirac point for the austenite phase state when geometric parameter $R = 10.55$ mm. (c) When the inversion center of unit cell is moved by $a/2$, this unit cell of austenite phase state is defined as type-II and its band structure and geometrical topological phase of Rayleigh waves are displayed.

Furthermore, to see the influence of filling factor on the topological properties of band gap, the two eigenfrequencys of surface wave changing with the radius R of semicircular block at the $k = \pi/a$ are demonstrated. Figure 3(a) shows the continuous evolution of the band-edge frequencies of surface wave at $k = \pi/a$ as a function of the parameter R when the SMA of NiTi is transformed to the full martensite. It can be seen that the band gap gradually closes and reopens through the critical point of $R = 10.85$ mm when the R ranges from 2.5 mm to 17.5 mm. Moreover, when R is 10.85 mm, the Dirac point of surface wave is formed at 7.543 kHz as shown in Fig. 3(b). At this case, the unit cell with Dirac point is defined as type-III. When R is less the 10.85 mm, the Zak phase of the band gap for the martensite is 0. And when R is more than 10.85 mm, the Zak phase of the band gap for the martensite is π. Obviously, there is no common region of bandgap with distinct Zak phase. To obtain the common topological bandgap, another kind of unit cell with a difference of half a lattice constant is built and defined as type-II as shown in the left panel of Fig. 3(c). Seeing from Fig. 3(c), the unit cell of type-II has the same band range as that of type-I, but they have the obvious bandgap with different Zak phases, indicating the distinct topological properties.

When the SMA of NiTi is transformed to the full austenite with a larger elastic modulus, the band structure and topological properties of the bandgaps for the unit cell of type-III and type-II are displayed in Fig. 4. Compared with the martensite phase state, the Dirac frequency of surface wave in austenite phase state for critical point with $R = 10.55$ mm increases to 8.553 kHz as shown in Figs. 4(a) and 4(b); and the topological bandgap shifts upwards to a higher frequency range as shown in Fig. 4(c).

2.3. Tunable TIS of Rayleigh wave

According to the topological properties of the surface wave bands, the Zak phases could be employed to determine the existence of the interface states located at the boundary between different structures in a common band gap.[25] Figure 5 illustrates the numerical model to calculate the tunable TIS of the surface wave, which is constructed by ten type-I unit cells possessed the Zak phase π of bandgap and ten type-II unit cells possessed the Zak phase 0 of bandgap to form the topological interface. The perfect matching layers (PML) are implemented on both ends and the low reflection boundary condition is added on the bottom to avoid the unnecessary reflections. The red dot located at the left side highlights the excited point source which is carried out by prescribing a displacement along y direction. And the red dot located at the right side highlights the received point to obtain the output signal. Besides, the transmission coefficient is defined as the ratio $S = 20\log_{10}(|u_y|_{(\text{out})}/|u_y|_{(\text{in})})$ where $|u_y|_{(\text{out})}$ is the absolute value of displacement component u_y at the received point and $|u_y|_{(\text{in})}$ is the absolute value of displacement component u_y at the input point.[50,51]

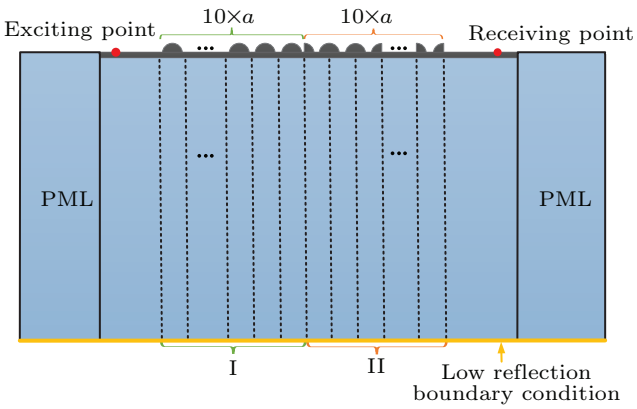


Fig. 5. The numerical model step to calculate the TIS of the topological Rayleigh waves, which are the composite structures I|II made up of the type-I and type-II PnCs when the SMA scatterers are in the martensite phase state and austenite phase state, respectively.

To demonstrate the tuning effect of the TIS for the surface wave, the transmission coefficients and displacement field distributions for the martensite phase state and austenite phase state are calculated as shown in Fig. 6. To standing out the transport property of the surface wave TIS, we perform the simulations for two kinds of the different models that one has the topological interface with combined I–II structure and the other is periodically arranged single I structure. Figures 6(a) and 6(d) display the transmission spectra of the two kinds of structures for the martensite phase state and austenite phase state, respectively. From the results, the sharp transmission peaks are clearly observed for the I–II structures in the common band gap, which are the TIS and both marked by the red arrows. However, for the martensite phase state, the frequency of the TIS is located at $f \approx 6.59$ kHz. And for the austenite phase state with the high temperature condition, the frequency of the TIS is located at $f \approx 7.55$ kHz. Performing the comparison between the frequency range of the transmission spectra in Figs. 6(a) and 6(d), a wonderful adjustable property of TIS for the proposed tunable topological surface wave PnCs. Meanwhile, figures 6(b) and 6(e) show the displacement field distributions of the surface wave TIS at the intermediate interface of I–II for the martensite phase state and austenite phase state, respectively. It can be seen that the surface wave displacement field distributions of the TIS are well confined at the interface, which exhibits a great potential for the capture of the surface acoustic wave energy. For a comparison, figures 6(c) and 6(f) also give the displacement field for the periodically arranged single type-I unit cell structure at the same frequency, in which we can see that there is no TIS due to the existence of the bandgap.

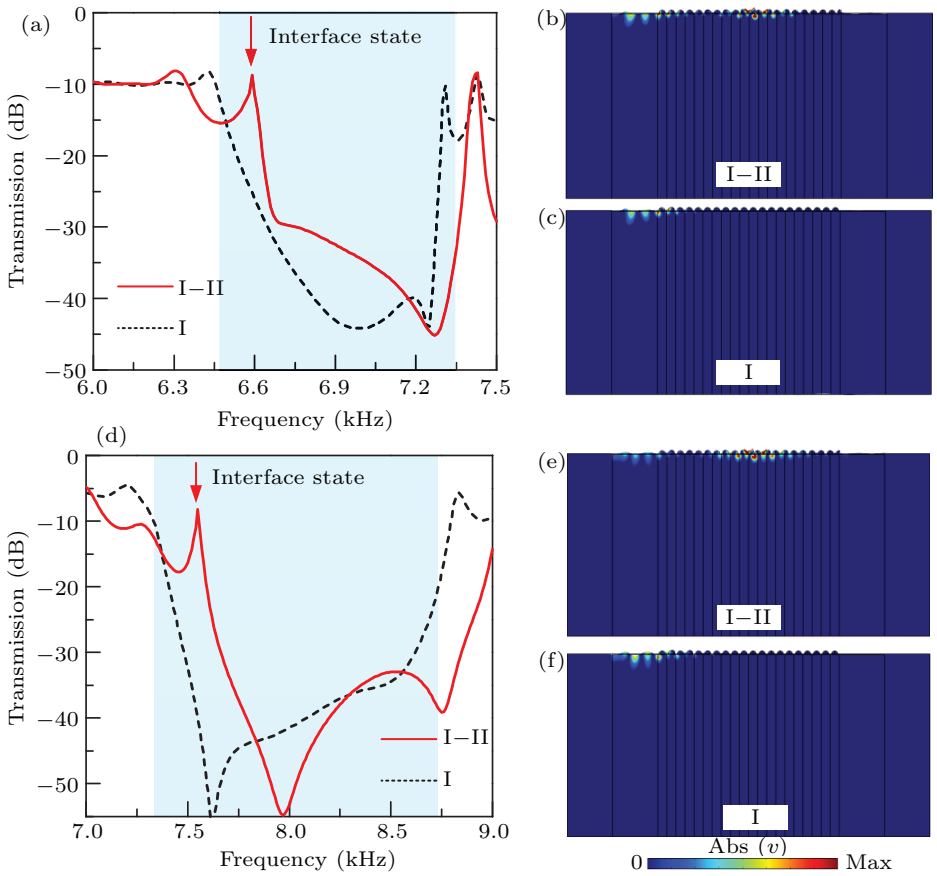


Fig. 6. (a) The calculated the transmission spectra of TIS for the composite PnCs structures I|II and single PnCs I when the SMA scatterers are in the martensite phase state. (b)–(c) The displacement field distribution of the interface state in the martensitic state for composite structures I|II and single PnCs I, respectively. (d) The calculated the transmission spectra of TIS for the composite PnCs structures I| II and single PnCs I when the SMA scatterers are in the austenitic phase state. (e)–(f) The displacement field distribution of the interface state in the austenitic state for composite structures I|II and single PnCs I, respectively.

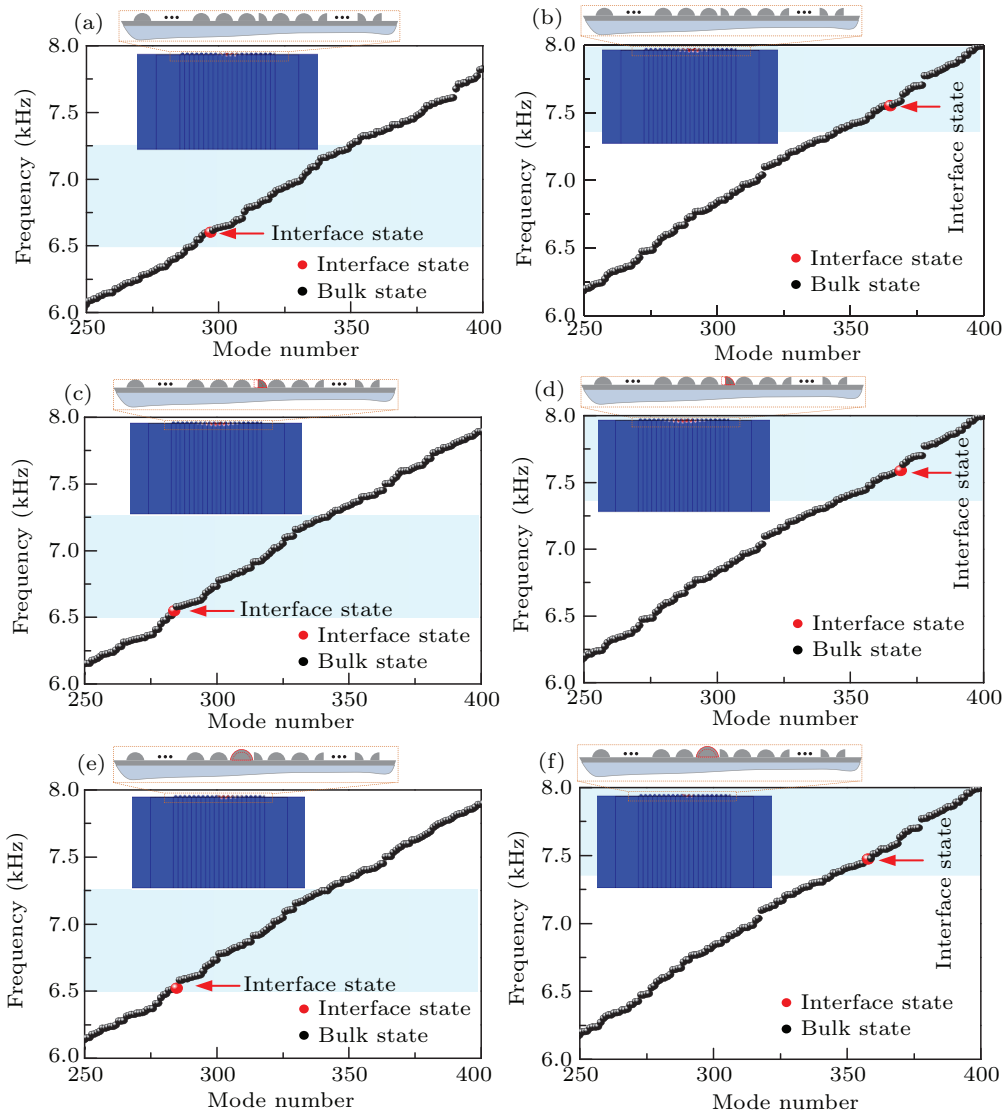


Fig. 7. (a)–(b) Eigenfrequency spectra of the surface wave PnCs for the martensite phase state and austenite phase state, respectively. (c)–(d) Eigenmodes profiles of the TIS when the defect is introduced in horizontal direction at the topological interface for the martensite phase state and austenite phase state, respectively. (e)–(f) Eigenmodes profiles of the TIS when the defect is introduced the vertical direction at the topological interface for the martensite phase state and austenite phase state, respectively.

The robustness against defects is the hallmark physical property of the topological states. Next, we further confirm the robustness of the TIS in the 1D surface wave PnCs as shown in Fig. 7. Firstly, we calculate the eigenfrequency spectrum for the topological structure without defects as shown in Figs. 7(a) and 7(b), whose results are in agreement with transmissions in Figs. 6(a) and 6(d). Then, we deliberately introduce the defects in horizontal direction by moving a small and random distance of $0.2a$ of the scatterer at the topological interface. The results are displayed in Figs. 7(c) and 7(d) for the martensite phase state and austenite phase state, respectively. The red dots presenting the positions of the TIS still keeps, indicating the robustness of the TIS when the random defects are introduced. Finally, a random defect is introduced along the vertical direction by increasing the radius of one scatterer to $1.2r$ at the interface to verify the robustness, and the eigenmodes profiles of the TIS as shown in Figs. 7(e) and 7(f).

3. Design of tunable TRS of Rayleigh wave with adjustable mode width

Inspired by the valley-lock waveguides with variable mode width in two-dimensional topological acosutic and photonic system,[52–54] we further extends the similar strategy to the 1D tunable topological surface wave to realize the tunable TRS of Rayleigh wave with adjustable mode width based on the concept of Zak phase instead of the topological valley Chern number.[52] The designed structure of surface wave TRS is shown in Fig. 8. By combining with two distinct 1D topological PnC I possessed Zak phase π of bandgap and PnC III possessed the Zak phase 0 of bandgap and the PnC III with Dirac point, we construct a sandwich-like structure $\mathrm{I}|\mathrm{III}_N|\mathrm{II}$, in which N represents the number of layers in type-III PnCs domain. The perfect matching layers (PML) are implemented on both ends and the low reflection boundary condition is added

on the bottom to avoid the unnecessary reflections. Similarly, the red dot located at the left side highlights the excited point source which is carried out by prescribing a displacement along *y* direction. And another red dot located at the right side highlights the received point to obtain the output signal.

Next, we perform the numerical simulations for the sandwich-like structure I|III$_N$|II to calculate the transmission spectra and displacement field distributions when the SMA material is being of the martensite phase state and austenite phase state, respectively. Figure 9 shows the obtained results for the full martensite phase state at the low temperature. When the layer number N of type-III PnCs is set 2, the transmission spectrum of the sandwich-like structure is shown in Fig. 9(a). It can be seen that a transmission peak occurs at the frequency of 6.82 kHz. The corresponding displacement field distribution of surface wave is shown in Fig. 9(d), in which the the surface wave energy is well confined in the domain III but prohibited in the domains I and II. This confining characteristic indicates that it is feasible to increase the mode width by arranging the 1D PnC with Dirac point into the middle of two 1D PnCs possessed different Zak phases of bandgap. To further illustrate this confining property, we increase the layer number N to 4 and 6. Figures 9(b) and 9(c) show the transmission spectra at $N = 4$ and $N = 6$, respectively. The TRS are located at the 7.05 kHz and 7.12 kHz. The corresponding displacement field distributions of surface waves are displayed in Figs. 9(e) and 9(f), respectively. It is obvious that the displacement field distributions are concentrated in the entire domain III and decays into domains I and II. Moreover, with the increasing of the layer number N, the frequencies of the TRS increase gradually. The above results indicate that the TRS of Rayleigh wave with adjustable mode width can be achieved by varying the layer number of the PnCs with Dirac point.

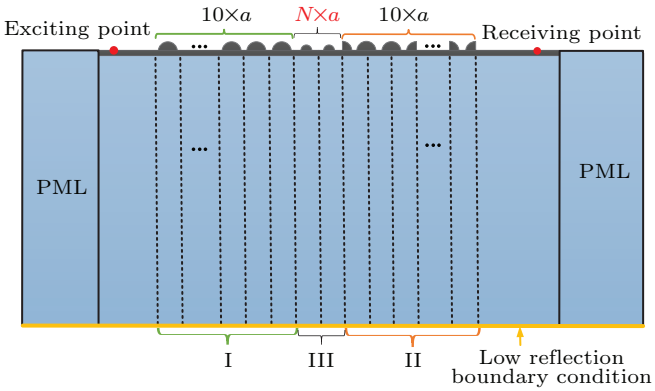


Fig. 8. The numerical model step to calculate the TRS of the topological Rayleigh waves, which are the sandwich-like structures I|III$_N$|II made up of the type-I, type-III, and type-II PnCs when the SMA scatterers are in the martensite phase state and austenite phase state, respectively.

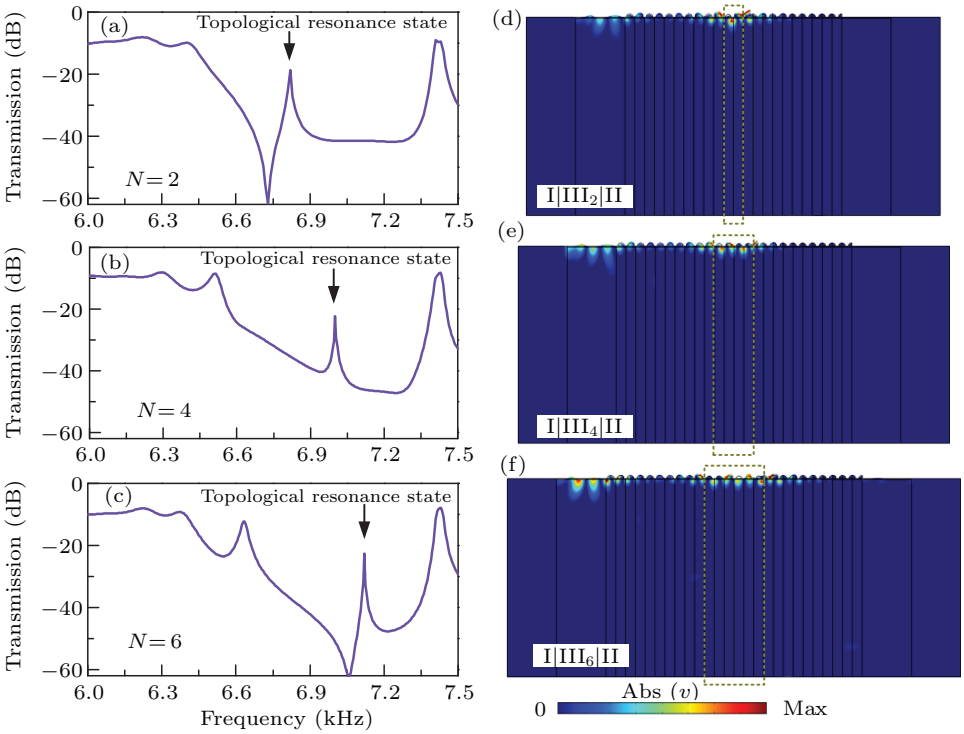


Fig. 9. The The calculated the transmission spectra of TRS for the sandwich structure I|III$_N$|II for the cases of (a) $N = 2$, (b) $N = 4$, and (c) $N = 6$, respectively, when the SMA scatterers of PnCs are in the martensite phase state. The corresponding displacement field distributions of TRS for $N = 2$, 4, and 6 are displayed in panels (d), (e), and (f), respectively.

To demonstrate the tuning effect of the TRS for the Rayleigh wave with tailorable mode width, we further study the transmissions and field distributions at the high temperature when the SMA material is being of full austenite phase state as shown in Fig. 10. The calculated transmission spectra of the sandwich-like structure I|III$_N$|II for $N = 2$, 4, and 6 are displayed in Figs. 10(a), 10(b), and 10(c), respectively. The corresponding TRS of the Rayleigh wave for $N = 2$, 4,

and 6 are located at frequency of 7.8 kHz, 7.99 kHz, and 8.11 kHz, which exhibits an upward trend with the number of layers. Figures 10(d), 10(e), and 10(f) show the displacement field distributions of the austenite phase for the layer number $N = 2$, 4, and 6, respectively, which also reflects a adjustable capacity of concentrating the surface wave energy. Compared with results from the case of the martensite phase state as shown in Fig. 9, the frequency of TRS from the the case of the austenite phase state as shown in Fig. 10 has an appreciable leap upward, which clearly embodies the tunable capability in the proposed surface wave PnCs by using the SMA material. Meanwhile, we note that the investigated TRS is different from the ordinary Fabry–Pérot (FP) resonance state. Unlike the FP cavity mode sensitive to defects,[55] the TRS in the topological system exhibits the robustness against the perturbations (see the supporting information). The presented investigations may pave the way for adaptive manipulation of the topological surface sensing and communications.

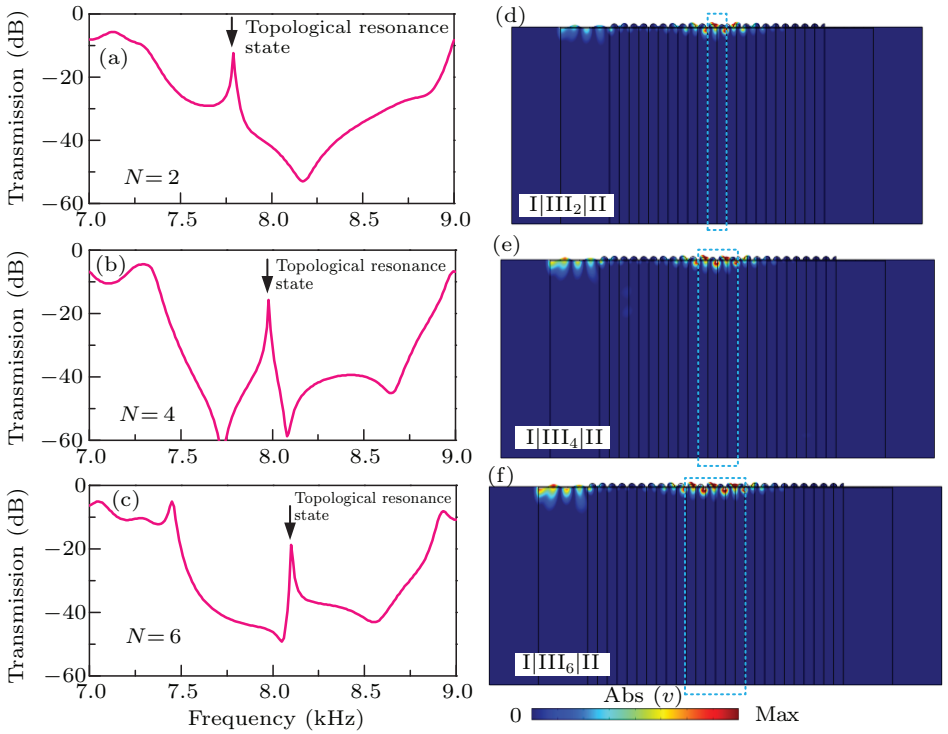


Fig. 10. The calculated the transmission spectrum of TRS for the sandwich structure I|III$_N$|II for the cases of (a) $N = 2$, (b) $N = 4$, and (c) $N = 6$, respectively, when the SMA scatterers of PnCs are being of the austenite phase state. The corresponding displacement field distributions of TRS for $N = 2$, 4, and 6 are displayed in panels (d), (e), and (f), respectively.

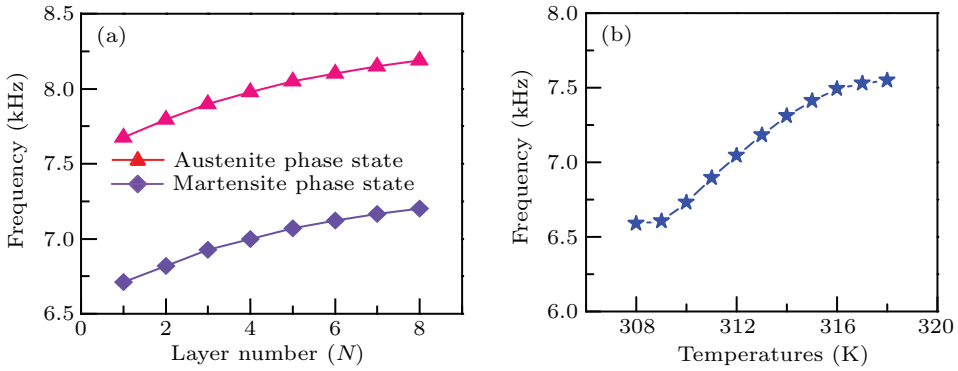


Fig. 11. (a) The evolution of the frequency for the TRS *versus* different temperature fields. (b) The evolution of the frequency for the TIS *versus* different temperature fields.

Lastly, to intuitively reflect the effects of layer number N and temperature T on the topological states, the frequency curves of the TRS corresponding to different layer number N with Dirac points and that of TIS corresponding to different temperature T are calculated as illustrated in Figs. 11(a) and 11(b), respectively. It can be seen that the layer number N with Dirac points not only confines the wave at a broader area but also shifts the frequency of TRS to higher positions. Meanwhile, from Fig. 11(b), it also can be seen that with increasing the temperature from 308 K to 318 K, the fully martensitic phase is gradually transited into the fully austenitic phases and the elastic modulus is gradually increased, which

leads to the increasing the frequency of the TIS. The results in Fig. 11 shows a flexible and adjustable ways for the manipulation of the topological surface wave. Besides, we have to refer to the experimental means to confirm the TIS and TRS for the Rayleigh surface wave. For the real experiment test, the sample can be fabricated by the LIGA-like technique[51,54] and mechanical machining. Two IDTs, act as surface acoustic waves emitter and receiver, respectively, are prepared on both sides and used to excited the surface acoustic waves and detect the transmission spectra. Moreover, a laser vibrometer imaged the out-of-plane displacement of the excited TIS, confirming the surface acoustic wave do strongly localized in the whole doping area, together with uniform phases. After the surface acoustic waves passed through the interfaces, they were captured by the receiver IDTs and read out by a vector network analyzer.[55] Combined the test on the transmittance and the displacement fields, the experiment test would be well carried out at the next research stage.

4. Conclusion

In this paper, an SMA-based tunable 1D surface wave PnCs with adjustable topological bandgap to obtain the TIS of Rayleigh wave has been proposed. The underlying mechanism originates from the unique elastic modulus change of the SMA material induced by the phase transformation under a temperature load. Significantly, based on the tunable TIS of Rayleigh wave, we have further designed a novel sandwich-like topological structure to realize the TRS with adjustable mode width in the 1D surface wave system by arranging the 1D PnC with Dirac point into the middle of two 1D PnCs possessed different Zak phases of bandgap. Compared with the interface hosting the TIS in previous literatures, our proposed sandwich-like structures hosting TRS are more flexible and controllable for interfacing with existing devices and applications due to the superiority of being simultaneously equipped with the tunable frequency-band range and the adjustable mode width. In a word, based on the phase transformation temperature of SMA in surface wave topological PnCs system, our work offers a new route for designing actively controllable topological surface sensing devices.

Acknowledgements

Project supported from the Doctoral Research Fund of University of South China (Grant No. 210XQD016) and the Outstanding Youth Foundation of the Hunan Education Department (Grant No. 21B0406).

References

[1] Thouless D J, Kohmoto M, Nightingale M P and den Nijs M 1982 *Phys. Rev. Lett.* **49** 405
[2] Bernevig B A, Hughes T L and Zhang S C 2006 *Science* **314** 1757
[3] Yang Z J, Gao F, Shi X H, Lin X, Gao Z, Chong Y D and Zhang B L 2015 *Phys. Rev. Lett.* **114** 114301
[4] Li F, Huang X Q, Lu J Y, Ma J H and Liu Z Y 2018 *Nat. Phys.* **14** 30
[5] Li R J, Lv B, Tao H B, Shi J H, Chong Y D, Zhang B L and Chen H S 2021 *Natl. Sci. Rev.* **8** nwaa192
[6] Li Y, Liu Y N and Zhang X 2020 *Chin. Phys. B* **29** 106301
[7] Yan M, Lu J Y, Li F, Deng W Y, Huang X Q, Ma J H and Liu Z Y 2018 *Nat. Mater.* **17** 993
[8] Chen Z G and Wu Y 2016 *Phys. Rev. Appl.* **5** 054021
[9] Ding Y G, Peng Y G, Zhu Y F, Fan X, Yang J, Liang B, Zhu X, Wan X and Cheng J C 2019 *Phys. Rev. Lett.* **122** 014302
[10] Geng Z G, Peng Y G, Shen Y X, Zhao D G and Zhu X F 2018 *Appl. Phys. Lett.* **113** 00350
[11] Xia B Z, Liu T T, Huang G L, Dai H Q, Jiao J R, Zang X G, Yu D J, Zheng S J and Liu J 2017 *Phys. Rev. B* **96** 094106
[12] Yu S Y, He C, Wang Z, Liu F K, Sun X C, Li Z, Lu H Z, Lu M H, Liu X P and Chen Y F 2018 *Nat. Commun.* **9** 1
[13] Wang W, Bonello B, Djafari-Rouhani B and Pennec Y 2019 *Phys. Rev. B* **100** 140101
[14] Mao H Y, Chen F J, Guo K and Guo Z Y 2021 *Chin. Phys. B* **30** 084302
[15] Pei D L, Yang T, Chen M and Jiang H 2019 *Chin. Phys. B* **28** 124301
[16] Nayak C, Simon S H, Stern A, Freedman M and Sarma S D 2008 *Rev. Mod. Phys.* **80** 1083
[17] Zhang Z W, Tian Y, Wang Y H, Gao S X, Cheng Y, Liu X J and Christensen J 2018 *Adv. Mater.* **180** 1803229
[18] Huang H B, Tan Z H, Huo S Y, Feng L Y, Chen J J and Han X 2020 *Commun. Phys.* **3** 46
[19] Zheng S J, Duan G J and Xia B Z 2020 *Int. J. Mech. Sci.* **174** 105463
[20] Aref T, Delsing P, Ekström M K, Kockum A F, Gustafsson M V, Johansson G, Leek P J, Magnusson E and Manenti R 2016 *Quantum Acoustics with Surface Acoustic Waves* (Cham: Springer) pp. 217–244
[21] Zeng Y, Zhang S Y, Zhou H T, Wang Y F, Cao L Y, Zhu Y F, Du Q J and Wang Y S 2021 *Mater. Des.* **208** 109906
[22] Chen Y, Liu H, Reilly M, Bae H and Yu M 2014 *Nat. Commun.* **5** 5247
[23] Zak J 1986 *Phys. Rev. Lett.* **62** 2747
[24] Su W P, Schrieffer J R and Heeger A J 1979 *Phys. Rev. Lett.* **42** 1698
[25] Xiao, M, Ma, G C, Yang, Z Y, Sheng, P, Zhang Z Q and Chan C T 2015 *Nat. Phys.* **11** 240
[26] Meng Y, Wu X X, Zhang R Y, Li X, Hu P, Ge L X, Huang Y Z, Xiang H, Han D Z, Wang S X and Wen W J 2018 *New J. Phys.* **20** 073032
[27] Fan L, Yu W W, Zhang S Y, Zhang H and Ding J 2016 *Phys. Rev. B* **94** 174307
[28] Huang H B, Chen J J and Huo S Y 2017 *J. Phys D: Appl. Phys.* **50** 275102
[29] Jin Y B, Wang W and Djafari-Rouhani B 2020 *Int. J. Mech. Sci.* **186** 105897
[30] Wang W, Jin Y B, Wang W, Bonello B, Djafari-Rouhani B and Fleury R 2020 *Phys. Rev. B* **101** 024101
[31] Zhou W J, Wu B, Chen Z Y, Chen W Q, Lim C W and Reddy J 2020 *J. Mech. Phys. Solids* **137** 103824
[32] Zhou W J, Chen W Q, Destrade M and Lim C W 2020 *Int. J. Mech. Sci.* **180** 105668
[33] Zhou W J, Muhammad, Chen W J, Chen Z Y and Lim C W 2019 *Eur. J. Mech.- ASolids* **77** 103807
[34] Chen Y J, Wu B, Li J, Rudykh S and Chen W Q 2021 *Int. J. Mech. Sci.* **191** 106098
[35] Wang H F, Liu D Y, Fang W B, Lin S Q, Liu Y J and Liang Y J 2020 *Int. J. Mech. Sci.* **176** 105549
[36] Feng L Y, Huang K, Chen J J, Luo J C, Huang H B and Huo S Y 2019 *AIP Adv.* **9** 115201
[37] Luo X H, Ren W J, Jin W and Zhang Z D 2009 *Chin. Phys. B* **26** 036501
[38] Liu Z H, Yi B, Li B T and Ma X Q 2021 *Acta Phys. Sin.* **61** 108104 (in Chinese)
[39] Tan C L, Tian X H and Cai W 2012 *Chin. Phys. B* **21** 057105
[40] Li P P, Wang J M and Jiang C B 2011 *Chin. Phys. B* **20** 028104
[41] Song R N, L X, Zhu W, Liu E K, Li G J, Cai J F, Wang W H and Wu G H 2012 *Acta Phys. Sin.* **61** 027501 (in Chinese)
[42] Shen H H, Yu H J, Fu H, Guo Y J, Fu Y Q and Zu X T 2011 *Chin. Phys. B* **20** 046102
[43] Chuang K C, Lv X F and Wang Y H 2019 *J. Appl. Phys.* **125** 055105
[44] Lv X F, Xu S F, Huang Z L and Chuang K C 2020 *Phys. Lett. A* **384** 126056

[45] Song YH and Shen Y F 2021 *Appl. Phys. Lett.* **118** 224104
[46] Ruzzene M and Baz A 2000 *J. Vib. Acoust.* **122** 151
[47] Liu S T and Mao Z X 2021 *Chin. J. Comput. Mech.* **38** 549
[48] Brinson L C 1993 *J. Intell. Mater. Syst. Struct.* **4** 229
[49] Xu M B and Song G 2004 *J. Sound Vib.* **278** 307
[50] Zhou W J and Fan Z 2021 *Smart Mater. Struct.* **30** 084001
[51] Zhang Z D, Yu S Y, Ge H, Wang J Q, Wang H F, Liu K F, Wu T, He C, Lu M H and Chen Y F 2021 *Phys. Rev. Appl.* **16** 044008
[52] Wang M D, Wang, Zhou W Y, Bi L Y, Qiu C Y, Ke M Z and Liu Z Y 2020 *Nat. Commun.* **11** 3000
[53] Chen Q L, Zhang L, Chen F J, Yan Q H, Xi R, Chen H S and Yang Y H 2021 *ACS Photon.* **8** 1400
[54] Wang J Q, Zhang Z D, Yu S Y, Ge H, Liu K F, Wu T, Sun X C, Liu L, Chen H Y, He C, Lu M H and Chen Y F 2022 *Nat. Commun.* **13** 1324
[55] Shao L B, Maity S, Zheng L, Wu L, Shams-Ansari A, Sohn Y, Puma E, Gadalla M N, Zhang M, Wang C, Hu E, Lai K J and Loncar M 2019 *Phys. Rev. Appl.* **12** 014022